Structure and transport properties of La0.5Sr0.5 − XCaxFeO3 − δ

ARTICLE *in* SOLID STATE IONICS · SEPTEMBER 2014

Impact Factor: 2.56 · DOI: 10.1016/j.ssi.2013.11.050

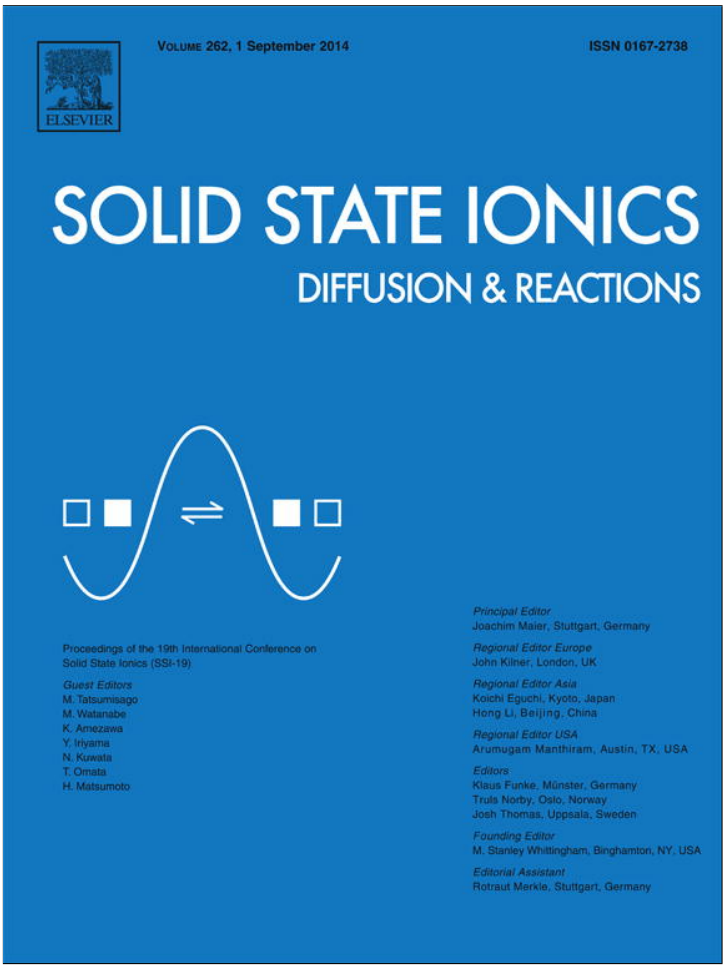

Solid State Ionics 262 (2014) 672–677

Contents lists available at ScienceDirect

Solid State Ionics

journal homepage: www.elsevier.com/locate/ssi

Structure and transport properties of $La_{0.5}Sr_{0.5-x}Ca_xFeO_{3-\delta}$

K.Yu. Chesnokov [a], A.A. Markov [a], M.V. Patrakeev [a,*], I.A. Leonidov [a,b], A.M. Murzakaev [b,c], O.N. Leonidova [a], E.V. Shalaeva [a,b], V.V. Kharton [d,e], V.L. Kozhevnikov [a]

[a] Institute of Solid State Chemistry, UB RAS, 91 Pervomayskaya Str., 620990 Ekaterinburg, Russia
[b] Ural Federal University, 19 Mira Str., 620002 Ekaterinburg, Russia
[c] Institute of Electrophysics, UB RAS, 106 Amundsen Str., 620016 Ekaterinburg, Russia
[d] Department of Materials and Ceramic Engineering, CICECO, University of Aveiro, 3810-193 Aveiro, Portugal
[e] Institute of Solid State Physics RAS, Chernogolovka 142432, Moscow District, Russia

ARTICLE INFO

Article history:
Received 16 May 2013
Received in revised form 25 November 2013
Accepted 28 November 2013
Available online 14 December 2013

Keywords:
Lanthanum-strontium ferrite
Mixed conductor
Perovskite
Vacancy ordering
Domain structure
Ion conductivity

ABSTRACT

Effects of calcium doping on the structure, dimensional stability, and mixed oxygen-ion and electron conductivity of perovskite-like $La_{0.5}Sr_{0.5-x}Ca_xFeO_{3-\delta}$ ($x = 0$–0.3) were studied in light of potential membrane applications. The incorporation of relatively small Ca^{2+} cations into the lanthanum-strontium ferrite lattice decreases unit cell volume, oxygen nonstoichiometry variations and chemical contribution to the thermal expansion in air. These changes correlate with rising tendency to local oxygen-vacancy ordering and the formation of nano-sized domains with the brownmillerite and $LaCa_2Fe_3O_8$-type lattices, as revealed by electron diffraction. The resultant vacancy trapping, changing domain structure and enlargement of the interfacial boundary area lead to non-linear relationships between the partial ion conductivity and cation composition, while the apparent activation energy for ion transport at temperatures below 900 °C remains almost constant, 0.6–0.7 eV. The n-type electron contribution to the total conductivity, measured in the oxygen pressure range 10^{-20}–0.5 atm at 700–950 °C, is also essentially independent of the calcium concentration.

1. Introduction

Dense oxide membranes with mixed oxygen-ion and electron conductivity make it possible to integrate oxygen separation from air and partial oxidation of methane to synthesis gas, a mixture of CO and H_2 [1–3]. The membrane materials should possess, in particular, fast ion and electron transport, thermodynamic and/or kinetic stability under both oxidizing and reducing conditions, stability with respect to CO_2 and H_2O, and moderate dimensional changes with temperature and oxygen partial pressure variations. The perovskite-like ferrites based on $(La,Sr)FeO_{3-\delta}$ seem to meet these requirements to a substantial extent [4–8]. The highest partial ion and electron conductivities in $La_{1-x}Sr_xFeO_{3-\delta}$ series are observed at $x = 0.5$ [6]. Moreover, tubular ceramic membranes of this composition provide a stable CH_4 conversion during over 7000 h [9].

Doping is a well-established approach to optimize functional properties of oxide materials. However, attempts to substitute Sr and Fe cations in $La_{0.5}Sr_{0.5}FeO_{3-\delta}$ result usually in lowering oxygen transport (e.g., [10–12]). Another possible approach may be based on the design of nanostructured composites where highly developed phase boundaries provide extra channels for the fast ion diffusion [13]. Grenier et al. [14] and Nemudry et al. [15] showed that complex perovskite-like ferrites tend to the separation of oxygen vacancy-ordered phases, leading to the formation of nanosized domain structures. This phenomenon may be of interest to transform an intrinsically homogeneous material, e.g. mixed-conducting $La_{0.5}Sr_{0.5}FeO_{3-\delta}$, into a nanostructured composite. In this context, the partial substitution of Ca^{2+} for Sr^{2+} may enable introducing structural inhomogeneities as calcium doping in $LaFeO_{3-\delta}$ and $SrFeO_{3-\delta}$ is known to promote oxygen-vacancy ordering [12,14,15]. The present work was centered on the synthesis, structural and microstructural analysis, and studies of electron-ion transport in the $La_{0.5}Sr_{0.5-x}Ca_xFeO_{3-\delta}$ system.

2. Experimental

Submicron powders of $La_{0.5}Sr_{0.5-x}Ca_xFeO_{3-\delta}$ ($x = 0.1$–0.3) were obtained using high-purity carbonates of calcium and strontium, lanthanum oxide and iron oxalate as the starting materials. The reagents were annealed at appropriate temperatures to remove absorbates, weighted in the stoichiometric proportions and dissolved in nitric acid. Then aminoacetic acid (50% excess to nitrates) was added to the solutions. The obtained viscous gels were heated in air with a gradual increase of temperature till their combustion. The products were calcined at 900 °C, re-ground, pelletized under 2 kbar uniaxial load and then sintered in air at 1300 °C for 10 h. The density of the obtained ceramics was approximately 93% of their theoretical density calculated employing full-profile refinement of X-ray diffraction (XRD) data. Reductive treatments of the powdered samples were carried out at

* Corresponding author. Tel.: +7 343 3623164; fax: +7 343 3744495.
E-mail address: patrakeev@ihim.uran.ru (M.V. Patrakeev).

0167-2738/$ – see front matter © 2013 Elsevier B.V. All rights reserved.
http://dx.doi.org/10.1016/j.ssi.2013.11.050

Table 1
Structural parameters of $La_{0.5}Sr_{0.5-x}Ca_xFeO_{3-\delta}$.

Composition	Space group	a (Å)	b (Å)	c (Å)	Reference
$La_{0.5}Sr_{0.5}FeO_{3-\delta}$	$R\bar{3}c$	5.503		13.417	[6]
$La_{0.5}Sr_{0.4}Ca_{0.1}FeO_{3-\delta}$	$R\bar{3}c$	5.502		13.383	This work
$La_{0.5}Sr_{0.3}Ca_{0.2}FeO_{3-\delta}$	*Pbnm*	5.466	5.500	7.731	This work
$La_{0.5}Sr_{0.2}Ca_{0.3}FeO_{3-\delta}$	*Pbnm*	5.469	5.473	7.715	This work

900 °C in flowing wet 95% He–5% H_2 gas mixture where the oxygen partial pressure (p_{O_2}) was approximately 10^{-14} atm. The local structure analysis was performed using a Jeol JEM 200CX electron microscope. The 4-probe d.c. conductivity measurements were performed in the oxygen partial pressure range 10^{-20}–0.5 atm at 700–950 °C as described elsewhere [16]. The total oxygen content was determined by thermogravimetry (TG) via complete reduction in a TG-DTA analyzer Setaram Setsys Evolution, which was also used to study oxygen nonstoichiometry variations in air. Dilatometric curves were collected employing a Linseis L75 instrument at atmospheric oxygen pressure.

3. Results and discussion

According to XRD results, the average structure of air-prepared $La_{0.5}Sr_{0.4}Ca_{0.1}FeO_{3-\delta}$ can be identified as rhombohedrally distorted perovskite (space group $R\bar{3}c$), as for parent $La_{0.5}Sr_{0.5}FeO_{3-\delta}$ [6]. Further additions of calcium lead to transition to the orthorhombic symmetry (S.G. *Pbnm*) typical for $La_{0.5}Ca_{0.5}FeO_{3-\delta}$ [17]. The unit cell parameters are summarized in Table 1. Note that calcium doping causes the unit cell volume contraction since Ca^{2+} cation radius (1.34 Å) is smaller than that of Sr^{2+}, 1.44 Å [18]. After the reductive treatments, XRD patterns of $La_{0.5}Sr_{0.5-x}Ca_xFeO_{3-\delta}$ were found to only exhibit peak characteristic of the cubic perovskite symmetry (S.G. $Pm\bar{3}m$), irrespective of calcium concentration.

The transmission electron microscopy (TEM) inspection revealed the features of underdeveloped vacancy ordering of the brownmillerite type in reduced $Sr_{0.3}La_{0.5}Ca_{0.2}FeO_{3-\delta}$. In addition to the fundamental reflections of the cubic perovskite phase, low-intensity diffuse effects, such as smeared spots and diffuse rods (streaks), were observed on some electron diffraction patterns (Figs. 1 and 2). The diffuse rods lie parallel to the $[010]_{cub}^*$ and $[001]_{cub}^*$ directions, and are centered at the $<0\ k+1/2\ l>_{cub}^*$ and $<0\ kl+1/2>_{cub}^*$ positions on the $[100]_{cub}$ diffraction patterns (Fig. 1a). Their positions thus coincide with the reciprocal lattice nodes of the brownmillerite phase if the two equivalent orientation relationships between the cubic perovskite and brownmillerite lattices are taken into consideration (Fig. 1b). The calculated combined electron diffraction patterns with the zone axis [100] show two typical variants of brownmillerite-type domains: $[010]_{br} \parallel [010]_{cub}$ and $[010]_{br} \parallel [001]_{cub}$. The observed distribution of the diffuse effects in $[100]_{cub}$ diffraction patterns is generally consistent with other diffraction patterns. It can be seen that there is only one set of diffuse rods on the diffraction pattern with zone axis close to $[320]_{cub}$ (Fig. 2a). The rods are parallel to $[001]_{cub}^*$ and are centered at the $<0\ 0\ l+1/2>_{cub}^*$ and $<2\ \bar{3}\ l+1/2>_{cub}^*$ positions. These diffuse rods belong to the reciprocal lattice of the brownmillerite domain with the orientation $[010]_{br} \parallel [001]_{cub}$, and correspond to the zone axis $\left[50\bar{1}\right]_{br}$ as shown by the calculated composite pattern (Fig. 2b). The two other sets of the diffuse rods, which are parallel to $[010]_{cub}^*$ and $[100]_{cub}^*$ and are related with the other two variants of the brownmillerite domains ($[010]_{br} \parallel [010]_{cub}$ and $[010]_{br} \parallel [100]_{cub}$), are inclined to the $[320]_{cub}$ cross-section. The intersection of these rods by the $[320]_{cub}$ plane gives the diffuse spots at the positions close to those calculated for the patterns with zone axes $\left[31\bar{3}\right]_{br}$ and $\left[43\bar{4}\right]_{br}$ (Fig. 2b). No diffraction spots of the zone axis $\left[31\bar{3}\right]_{br}$ close to perovskite reflections $(2\bar{3}l)$ were observed on the experimental patterns, a result of low intensity of these reflections and inexact $[320]_{cub}$ zone axis orientation.

In addition, weak diffuse spots are visible on the experimental $[320]_{cub}$ pattern, which do not belong to any brownmillerite cross-sections exactly coinciding with the $[320]_{cub}$ pattern. These include two rows of diffuse spots, which are parallel to and equidistant from the reflection rows $(00l)_{cub}$ and $(2\bar{3}l)_{cub}$, as well as some spots of the type $(2/2\ \bar{3}/2\ (l+1/2)/2)$ (Fig. 2a, shown by arrows). As indicated by the calculated composite diffraction pattern, all these diffuse sports can belong to the $\left[11\bar{1}\right]$ zone axis of a small domain of the $Ca_2LaFe_3O_8$-like

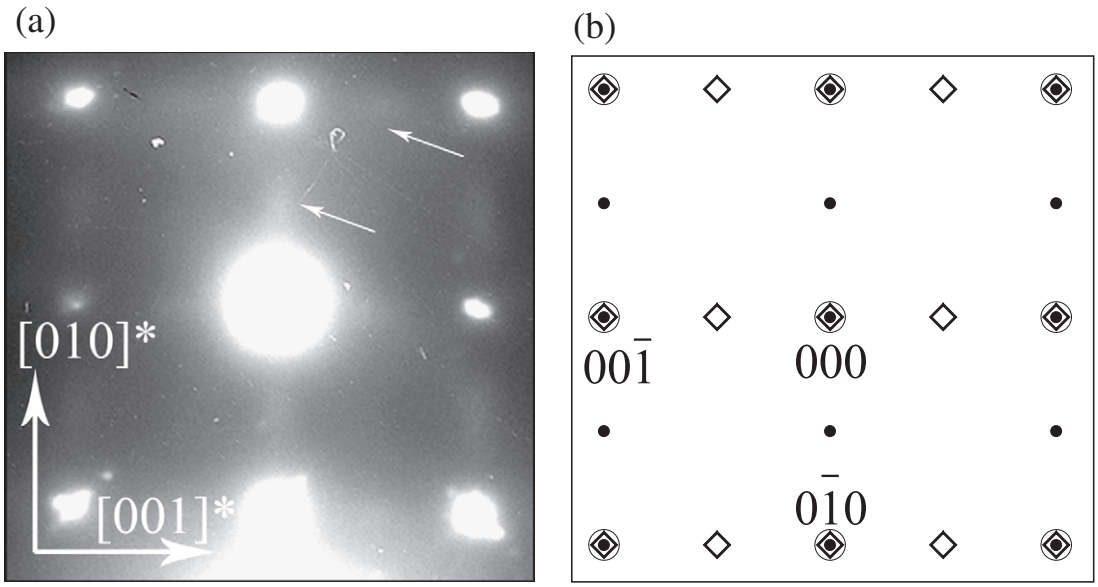

Fig. 1. Selected area electron diffraction (SAED) patterns for reduced $Sr_{0.5}La_{0.3}Ca_{0.2}FeO_{3-\delta}$: a—zone axis $[100]_{cub}$ diffuse rods, centered at $<0\ k+1/2\ l>_{cub}^*$ and $<0\ kl+1/2>_{cub}^*$ positions (shown by arrows); b—simulated composite diffraction pattern for the brownmillerite-type domain structure with zone axis $[010]_{br}$ (diamond) and $\left[10\bar{1}\right]_{br}$ (dark circle) parallel to $[100]_{cub}$. The strongest reflections are indexed for the cubic perovskite phase.

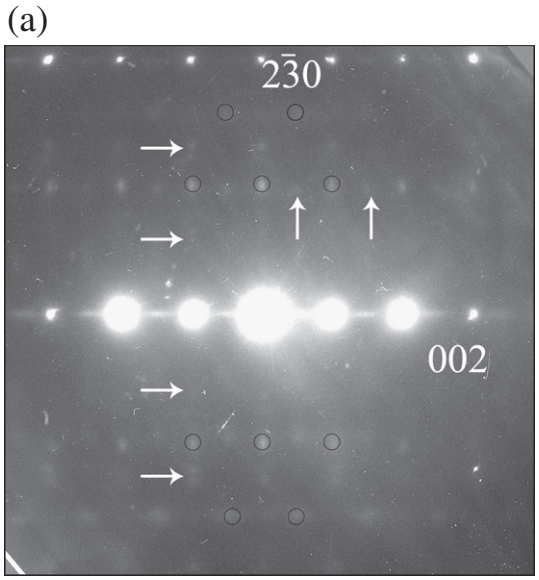

(C2LF3) phase, Fig. 2c. Furthermore, these effects may result from the intersection of the nearest brownmillerite diffuse rods centered at the $\langle h + 1/2\ kl\rangle_{cub}^*$ positions with the Ewald sphere due to their elongated shape. Both kinds of domains with the $Ca_2LaFe_3O_8$- and brownmillerite-like structures can give very closely spaced diffuse spots of this type, that are indeed observed in some cases (Fig. 2a).

Therefore, the observed diffraction effects for reduced $Sr_{0.3}La_{0.5}Ca_{0.2}FeO_{3-\delta}$ can be attributed mainly to the reciprocal lattice of the brownmillerite domain structure, while $\langle 010\rangle_{br}^*$ is at the reciprocal lattice nodes. The diffuse rods, which seem parallel to the $\langle 010\rangle_{br}^*$ reciprocal lattice vectors, indicate that brownmillerite phase is still poorly ordered and the interplanar disorder from $(010)_{br}$ layers is more pronounced than disorder in the structural layers. Note that the interplanar disorder is typical for the oxygen vacancy layers in the brownmillerite structure [14]. The smallest size of the regions where ordered arrangement of the layers takes place in the direction $\langle 010\rangle_{br}$, was estimated from the length of the diffuse rods accounting for the finite crystal-size effect and corresponds to approximately 1.5–2.0 nm. The formation of nanosized $Ca_2LaFe_3O_8$ type domains cannot be ruled out as well. Hence, the electron diffraction studies reveal that vacancy ordering of the brownmillerite and $Ca_2LaFe_3O_8$ types occurs only in nano-scale regions of the perovskite phase with the most pronounced interlayer disorder. Intergrowths of well-ordered $Ca_2LaFe_3O_8$-like phase are rarely observed in reduced $Sr_{0.3}La_{0.5}Ca_{0.2}FeO_{3-\delta}$ (Fig. 3). Reduced $Sr_{0.2}La_{0.5}Ca_{0.3}FeO_{3-\delta}$ with higher concentration of calcium was found to contain a larger number of crystallites of the cubic perovskite phase, which exhibit no diffuse brownmillerite-type reflections. At the same time, the content of ordered $Ca_2LaFe_3O_8$-like domains increases with calcium additions. Fig. 4a shows one example of the $[110]_{cub}$ electron diffraction pattern obtained for $Sr_{0.2}La_{0.5}Ca_{0.3}FeO_{3-\delta}$. The superstructural reflections can be seen in the positions coinciding with the reciprocal lattice nods of the ordered $Ca_2LaFe_3O_8$-like phase if the intergrowths have the following orientation: $[100]_{C2LF3} \parallel [110]_{cub}$; $[010]_{C2LF3} \parallel [001]_{cub}$. This is confirmed by the calculated combine diffraction pattern (Fig. 4b). The fine $[010]_{C2LF3}^*$ diffuse streaks going through the $Ca_2LaFe_3O_8$-like phase reflections, reveal that along $[010]_{C2LF3}$ direction $Ca_2LaFe_3O_8$ intergrowths are very thin. Again, these structural features are typical of $Ca_2LaFe_3O_8$-phase intergrowths [19]. One should also note weak reflections in the $\langle 1/2\ 1/2\ 1/2\rangle_{cub}^*$ type positions. Such reflections were often observed on the diffraction patterns of $La_{0.5}Sr_{0.5-x}Ca_xFeO_{3-\delta}$ with $x = 0.2$–0.3 and are associated with starting double-perovskite ordering in the A cation sublattice, since the ionic radius difference between La^{3+} and Ca^{2+} is quite large.

TG measurements demonstrated that calcium doping reduces reversible variations of the oxygen content at atmospheric oxygen pressure, which is clearly visible for the material with $x = 0.3$ (Fig. 5a). This tendency results in a lower chemical contribution to apparent thermal expansion, Fig. 5b. Taking into account the electron diffraction data, such behavior can be unambiguously attributed to the formation of the vacancy-ordered domains with essentially fixed oxygen content. It should also be mentioned that, in addition to the lower oxygen-nonstoichiometry variations, the thermal and chemical expansion of the layered perovskite-like ferrites such as brownmillerite or Ruddlesden–Popper type phases is considerably lower compared to their disordered perovskite analogs [20–22].

Fig. 2. SAED patterns for reduced $Sr_{0.5}La_{0.3}Ca_{0.2}FeO_{3-\delta}$: a—close to zone axis $[320]_{cub}$, b—simulated composite diffraction patterns for the brownmillerite-type domain structure: zone axis $[50\bar{1}]_{br}$ (diamond); $[31\bar{3}]_{br}$ (dark circle); $[43\bar{4}]_{br}$ (cross) parallel to $[320]_{cub}$; squares designate diffuse spots (shown on diffraction pattern by arrows) that appear due to the diffuse rods, centered at the nearest $\langle h + 1/2\ kl\rangle_{cub}^*$ positions (brownmillerite domain with orientation $[010]_{br} \parallel [100]_{cub}$), intersecting Ewald sphere. The strongest reflections are indexed for the cubic perovskite; c—simulated composite diffraction pattern for $Ca_2LaFe_3O_8$ domain and perovskite structure, $[11\bar{1}]_{C2LF3}$ zone axis parallel to $[320]_{cub}$, $Ca_2LaFe_3O_8$ phase reflections are indexed.

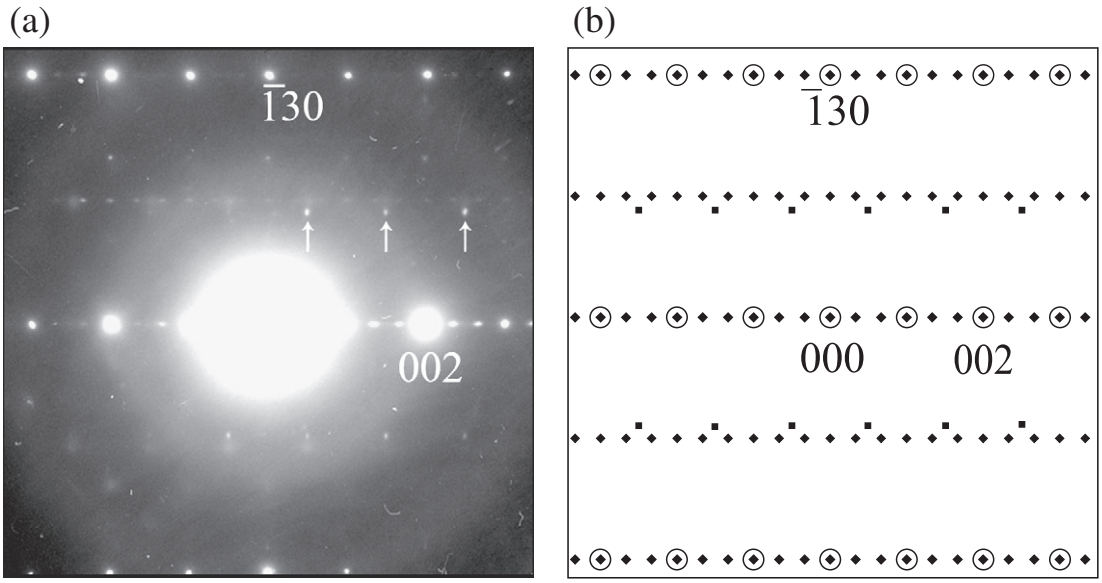

Fig. 3. SAED pattern of $Sr_{0.3}La_{0.5}Ca_{0.2}FeO_{3-\delta}$, zone axis $[310]_{cub}$ (a), and simulated composite diffraction patterns for cubic perovskite and intergrowths of $Ca_2LaFe_3O_8$-like phase (b), zone axis $\left[20\bar{1}\right]_{C2LF3}$ parallel to $[310]_{cub}$. Arrows show the reflections of zone axis $\left[92\bar{9}\right]_{C2LF3}$, that intersect Ewald sphere due to their elongated shape. The strongest reflections are indexed for the cubic perovskite.

The oxygen partial pressure dependencies of the total conductivity of $La_{0.5}Sr_{0.5-x}Ca_xFeO_{3-\delta}$ are presented in Fig. 6. The plots exhibit smooth minima at the oxygen chemical potentials corresponding to the so-called intrinsic electron-hole equilibrium, when the concentrations of p- and n-type electronic charge carriers are equal and the average oxidation state of iron cations is 3+. The total conductivity (σ) variations in the vicinity of these minima can be approximated by the classical relationship:

$$\sigma = \sigma_i + \sigma_n^0 \cdot p_{O_2}^{-\frac{1}{4}} + \sigma_p^0 \cdot p_{O_2}^{+\frac{1}{4}} \quad (1)$$

where σ_i is the oxygen ion contribution p_{O_2}-independent in the given oxygen-pressure range due to almost constant vacancy concentration under reducing conditions [1,3,6,10,16], and σ_n^0 and σ_p^0 are the electron and hole contributions at $p_{O_2} = 1$ atm, respectively. The fitting results shown in Fig. 6 by solid lines are in excellent agreement with the experimental data. The statistical errors of the calculated σ_i, σ_n^0 and σ_p^0 values are lower than 2, 4 and 5%, correspondingly. The Arrhenius plots of the calculated ion and *n*-type electron conductivities are shown in Fig. 7(a and b). At temperatures below 900 °C, the apparent activation energy for ion transport in reducing atmospheres is essentially independent of *x* and varies in the range 0.6–0.7 eV. On the contrary, absolute values of the ion conductivity are substantially affected by doping. For the composition with relatively low calcium content, $x = 0.1$, the ion conductivity is approximately 1.5 times smaller compared to parent $La_{0.5}Sr_{0.5}FeO_{3-\delta}$. For $x = 0.2$, the σ_i values increase and become similar to those at $x = 0$; further additions of calcium

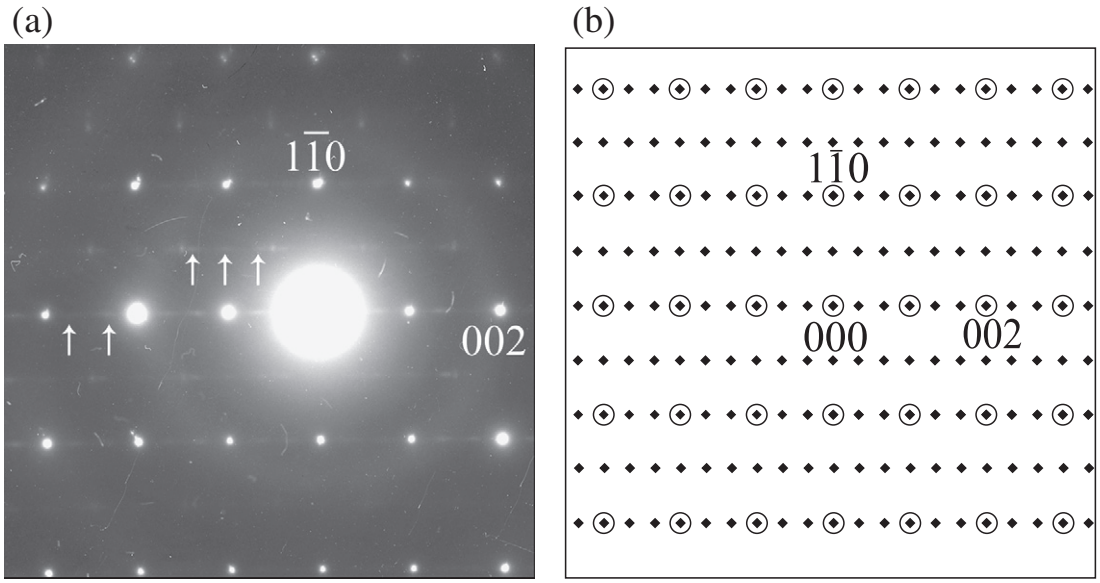

Fig. 4. SAED pattern of reduced $Sr_{0.2}La_{0.5}Ca_{0.3}FeO_{3-\delta}$, zone axis $[110]_{cub}$ (a), and simulated composite diffraction patterns for cubic perovskite and intergrowths (b), zone axis $[100]_{C2LF3}$ parallel to $[310]_{cub}$. Arrows show reflections of $Ca_2LaFe_3O_8$-like phase. The strongest reflections are indexed for cubic perovskite.

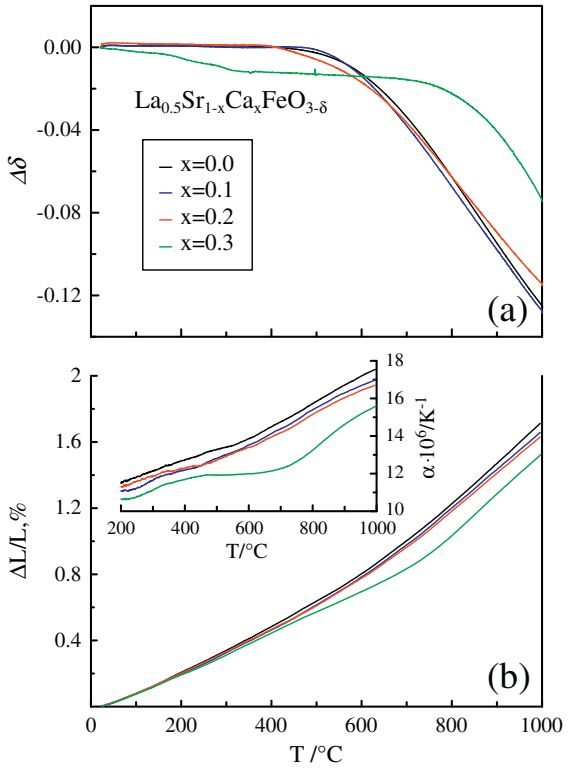

Fig. 5. Temperature dependencies of the oxygen nonstoichiometry variations (a) and relative elongation (b) of $La_{0.5}Sr_{0.5-x}Ca_xFeO_{3-\delta}$ ceramics. The inset shows thermal expansion coefficients (TECs). All data correspond to atmospheric air.

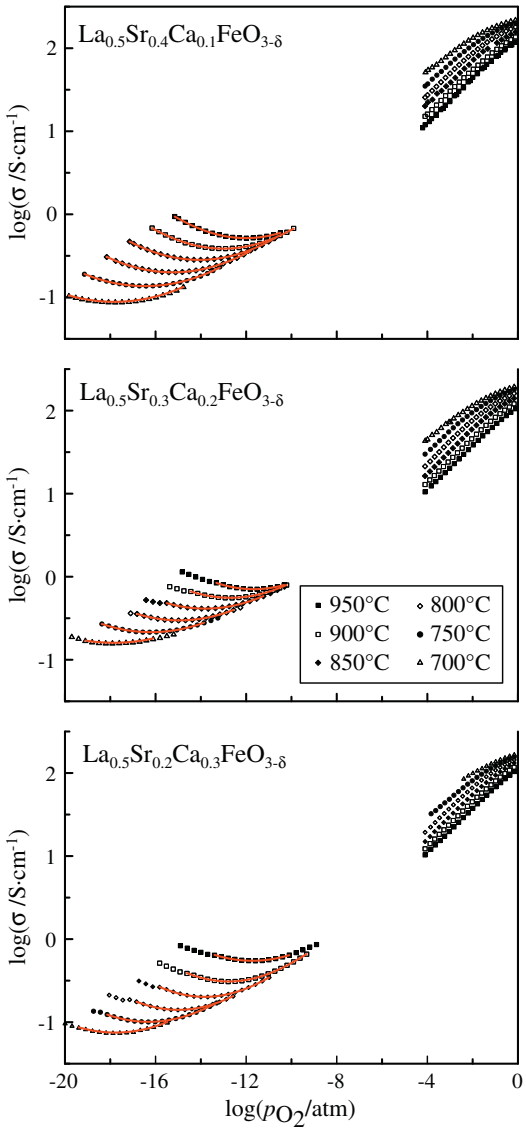

Fig. 6. Oxygen partial pressure dependencies of the total conductivity of $La_{0.5}Sr_{0.5-x}Ca_xFeO_{3-\delta}$ at 700–950 °C. Solid lines correspond to the fitting results using Eq. (1) as the regression model. The intermediate p_{O_2} region is omitted due to kinetic limitations.

and resultant changes in the domain structure lead to a dramatic conductivity drop and to an appearance of the activation energy changes at 850–950 °C, characteristic of massive order–disorder transition in the oxygen sublattice.

This unusual behavior is qualitatively consistent with the structural data, indicating that the ion transport variations induced by Ca^{2+} doping are governed by several competing factors, namely the charge-carrier concentration and mobility in the perovskite phase, interfacial boundary area, and vacancy-ordered domain size and composition. The first group of oxygen diffusivity-determining factors includes decreasing fraction of mobile oxygen vacancies due to their trapping in the ordered nanodomains, and decreasing vacancy mobility owing to the perovskite lattice contraction on doping with relatively small Ca^{2+}. These effects, well-known for essentially disordered perovskite ferrites, such as $(La,Sr)FeO_{3-\delta}$ [4–6], seem responsible for lowering ionic conductivity at modest additions of calcium ($x = 0.1$). Second, the increase of the interfacial boundary area originating from the appearance of numerous nanodomains at $x = 0.2$ is assumed to promote ion diffusion. As shown by the electron diffraction studies, increasing calcium content up to $x = 0.2$ results in massive formation of the locally ordered domains with the brownmillerite and $Ca_2LaFe_3O_8$ structures. The increase in the ion conductivity observed at $x = 0.2$ cannot be ascribed to the major perovskite phase where any local changes in the acceptor-type dopant concentration could not increase ion conductivity [6]. Moreover, this behavior cannot also originate from the bulk transport in the domains with the vacancy-ordered structures, since ion conduction in the ordered ferrites is, as a rule, significantly lower compared to the disordered perovskite analogs [1,12,14–16]. On the contrary, the formed interfacial boundaries provide extra channels for ion diffusion, which becomes moderately faster. Similar positive impact of highly developed phase boundary between the brownmillerite-type domains and disordered perovskite domains was detected in previous works [23,24].

Finally, the growth of $LaCa_2Fe_3O_8$-based domains leading to the interfacial boundary contraction and lowering the content of $Sr_2Fe_2O_5$-type phase at $x = 0.3$ have negative impact on the anion transport. The relevant role of the former process seems supported by the sharp increase of ion conduction activation energy in $La_{0.5}Sr_{0.2}Ca_{0.3}FeO_{3-\delta}$ above 850 °C, which is characteristic of thermal disordering and may only become possible when the size and fraction of the vacancy-ordered domains are large enough. Notice that experimental findings and hypotheses described above are in agreement with the theoretical analysis of ion diffusivity in nanostructured composite systems (Ref. [13] and references therein). At the same time, our assumptions enable only qualitative explanation of the observed behavior and should be experimentally validated in the future, including identification of the microscopic transport mechanisms.

Another trend important for potential practical applications of the title materials was observed for the n-type electron conductivity, almost independent of calcium content (Fig. 7b). In combination with decreasing thermal and chemical expansion (e.g. Fig. 5b), this feature makes it possible to develop novel materials for solid oxide fuel cell (SOFC)

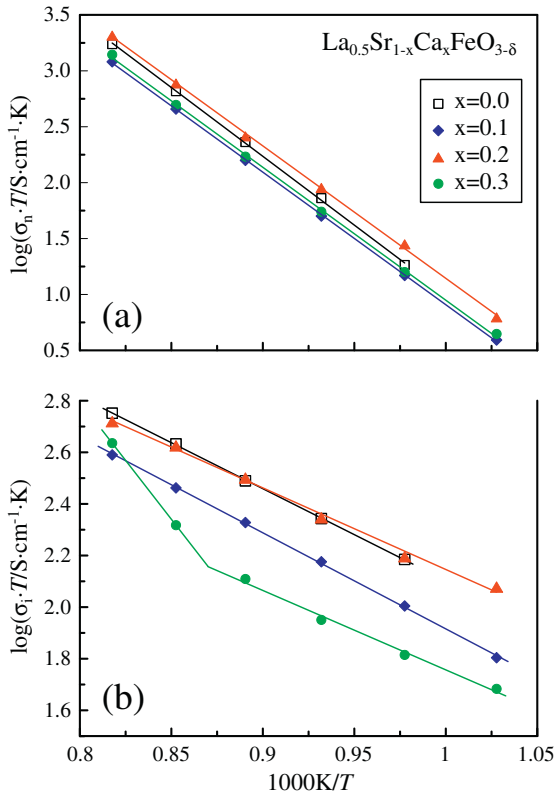

Fig. 7. Arrhenius plots for the partial n-type electron conductivity at $p_{O_2} = 10^{-16}$ atm (a) and ion conductivity (b) in $La_{0.5}Sr_{0.5-x}Ca_xFeO_{3-\delta}$. The data for $x = 0$ are taken from Ref. [6].

anodes where the electron transport and dimensional stability are among most critical requirements, via further compositional optimization of nano-heterogeneous ferrites.

4. Conclusion

The crystal structure, oxygen nonstoichiometry, thermochemical expansion and transport properties of perovskite-like $La_{0.5}Sr_{0.5-x}Ca_xFeO_{3-\delta}$ ($x = 0$–0.3) were studied in order to appraise effects of calcium doping. These effects are associated with relatively small radius of Ca^{2+}, leading to the lattice contraction and extensive oxygen-vacancy ordering. As a result, the oxygen nonstoichiometry variations induced by changes in temperature or oxygen chemical potential, and thermochemical expansion of the ceramic materials decrease on doping, while the n-type electron conductivity remains essentially unchanged. The relationships between Ca^{2+} content and ion conductivity are nonlinear, suggesting an important role of interfacial transport processes at the domain boundaries. As the ion conductivity of $La_{0.5}Sr_{0.3}Ca_{0.2}FeO_{3-\delta}$ is similar to that of parent $La_{0.5}Sr_{0.5}FeO_{3-\delta}$, the former composition may be of interest for practical applications in the membrane reactors for partial oxidation of light hydrocarbons.

Acknowledgments

This work was partially funded by the Ministry of Education and Science of the Russian Federation (grants No. 8649 and 14.B25.31.0018), the Russian Foundation for Basic Research (13-03-00931-a), and the FCT, Portugal. The authors are also grateful to the Ural Branch of RAS for the support of this study through the regional programs (12-Y-3-1005 and 12-3-2-002 Arctic).

References

[1] H.J.M. Bouwmeester, A.J. Burggraaf, in: A.J. Burggraaf, L. Cot (Eds.), Fundamentals of Inorganic Membrane Science and Technology, Elsevier, Amsterdam, 1996, p. 435.
[2] Y. Liu, X. Tam, K. Li, Catal. Rev. 48 (2006) 145–198.
[3] In: V.V. Kharton (Ed.), Solid State Electrochemistry II: Electrodes, Interfaces and Ceramic Membranes, Wiley-VCH, Weinheim, 2011.
[4] J. Mizusaki, T. Sasamo, W.R. Cannon, H.K. Bowen, J. Am. Ceram. Soc. 66 (1983) 247–252.
[5] J.E. ten Elshof, H.J.M. Bouwmeester, H. Verweij, Solid State Ionics 89 (1996) 81–92.
[6] M.V. Patrakeev, J.A. Bahteeva, E.B. Mitberg, I.A. Leonidov, V.L. Kozhevnikov, K.R. Poeppelmeier, J. Solid StateChem. 172 (2003) 219–231.
[7] A. Fossdal, M. Menon, I. Waernhus, K. Wiik, M.A. Einarsrud, T. Grande, J. Am. Ceram. Soc. 87 (10) (2004) 1952–1959.
[8] Y. Wei, W. Yang, J. Caro, H. Wang, Chem. Eng. J. 220 (2013) 185–203.
[9] A.A. Markov, M.V. Patrakeev, I.A. Leonidov, V.L. Kozhevnikov, J. Solid State Electrochem. 15 (2011) 253–257.
[10] V.V. Kharton, J.C. Waerenborgh, A.P. Viskup, S.O. Yakovlev, M.V. Patrakeev, P. Gaczyński, I.P. Marozau, A.A. Yaremchenko, A.L. Shaula, V.V. Samakhval, J. Solid State Chem. 179 (2006) 1273–1284.
[11] D. Bayraktar, S. Diethelm, P. Holtappels, T. Graule, J. Van herle, J. Solid State Electrochem. 10 (2006) 589–596.
[12] V.V. Kharton, A.V. Kovalevsky, M.V. Patrakeev, E.V. Tsipis, A.P. Viskup, V.A. Kolotygin, A.A. Yaremchenko, A.L. Shaula, E.A. Kiselev, J.C. Waerenborgh, Chem. Mater. 20 (2008) 6457–6467.
[13] J. Maier, Solid State Ionics 157 (2003) 327–334.
[14] J.-C. Grenier, M. Pouchard, P. Hagenmuller, Struct. Bond. 47 (1981) 1–25.
[15] A. Nemudry, I. Rogatchev, R. Gainutdinov, J. Schöllhorn, Solid State Electrochem. 5 (2001) 450–458.
[16] I.A. Leonidov, V.L. Kozhevnikov, E.B. Mitberg, M.V. Patrakeev, V.V. Kharton, F.M.B. Marques, J. Mater. Chem. 11 (2001) 1201–1208.
[17] M. Takano, Mater. Res. Bull. 12 (1977) 923.
[18] R.D. Shannon, Acta Crystallogr. Sect. A 32 (1976) 751–767.
[19] M.A. Alario-Franco, J.M. Gonzalez-Calbet, M. Vallet-Regi, J. Solid State Chem. 49 (1983) 219–231.
[20] M.V. Patrakeev, I.A. Leonidov, V.L. Kozhevnikov, V.V. Kharton, Solid State Sci. 6 (2004) 907–913.
[21] A.L. Shaula, Y.V. Pivak, J.C. Waerenborgh, P. Gaczyński, A.A. Yaremchenko, V.V. Kharton, Solid State Ionics 177 (2006) 2923–2930.
[22] V.V. Kharton, M.V. Patrakeev, E.V. Tsipis, M. Avdeev, E.N. Naumovich, P.V. Anikina, J.C. Waerenborgh, Solid State Ionics 181 (2010) 1052–1063.
[23] P.V. Anikina, A.A. Markov, M.V. Patrakeev, I.A. Leonidov, V.L. Kozhevnikov, Solid State Sci. 11 (2009) 1156–1162.
[24] A.A. Markov, O.A. Savinskaya, M.V. Patrakeev, A.P. Nemudry, I.A. Leonidov, Yu.T. Pavlyukhin, A.V. Ishchenko, V.L. Kozhevnikov, J. Solid State Chem. 182 (2009) 799–806.